An investigation of unsteady 3D effects on trailing edge flaps

Eva Jost[1], Annette Fischer[1], Galih Bangga[1], Thorsten Lutz[1], and Ewald Krämer[1]

[1]Institute of Aerodynamics and Gas Dynamics, University of Stuttgart, Pfaffenwaldring 21, 70569 Stuttgart, Germany

Correspondence to: Eva Jost (e.jost@iag.uni-stuttgart.de)

Abstract. The present study investigates the impact of unsteady 3D aerodynamic effects on a wind turbine blade with trailing edge flap by means of Computational Fluid Dynamics (CFD). Harmonic oscillations are simulated on the DTU 10 MW rotor with a morphing flap of 10% chord extent ranging from 70% to 80% blade radius. The deflection frequency is varied in the range between 1p and 6p. To quantify 3D effects, rotor simulations are compared to 2D airfoil computations and the 2D theory by Theodorsen. A significant influence of trailing and shed vortex structures has been found which leads to an amplitude reduction and hysteresis of the lift response in the flap section with regard to the deflection signal. For the 3D rotor results greater amplitude reductions and a less pronounced hysteresis is observed compared to the 2D airfoil case. Blade sections neighboring the flap experience however an opposing impact and hence partly compensate the negative effect of trailing vortices in the flap section in respect to integral loads. The comparison to steady flap deflections at the 3D rotor revealed the high influence of dynamic inflow effects.

1 Introduction

The reduction of ultimate and fatigue loads plays an important role in today's wind energy research. In the background of economic efficiency, load alleviation systems bare potential to reduce rotor weight and costs, to increase the turbine reliability or allow a further enlargement of the rotor radius and thus power output. One promising concept to reduce dynamic load fluctuations are trailing edge flaps applied to the outer part of the rotor blade. As flaps are able to increase or decrease the local lift by adapting the deflection angle, it is possible to partly compensate load variations due to variations of the effective inflow angle and velocity.

Over the last years several investigations showed the potential of the flap concept as for example a test on a full-scale turbine performed by Castaignet et al. (2014). In aeroelastic simulations fatigue load reductions up to approximately 30 % have been found for a trailing edge flap covering up to 25 % of the blade span of a 5 MW turbine (Barlas et al., 2012). In most of the numerical studies the aerodynamic loading was computed by blade element momentum (BEM) codes, which have been extended with different engineering models to account for the unsteady flow. As viscous and unsteady aerodynamics have a great influence on dynamically deflected flaps, it is however important to also apply higher fidelity models and gain knowledge of the flow physics. A recent benchmarking (Jost et al., 2015a) showed that there are still differences between the results of CFD simulations and BEM methods which need to be analyzed. While a previous investigation focused on the analysis of static

flap deflection angles (Jost et al., 2016) by means of CFD, the main objective of the present work is to study the influence of unsteady 3D effects on the example of harmonically oscillating morphing flaps.

Different deflection frequencies ranging from 1p to 6p are analyzed on the DTU 10 MW rotor (Bak et al., 2013) at rated operational condition. These frequencies are considered a realistic operational range for active load alleviation. The investigated
5   flap layout consists of a single morphing flap ranging from 70% to 80 % blade radius with 10 % local chord extent. This limited dimension along the blade span was chosen to obtain a high impact of 3D effects. In all cases the flap oscillates with an amplitude of $10°$.

2   Aerodynamic effects of trailing edge flaps

A qualitative illustration of the vortex development around a rotor blade with deflected flap can be given on the basis of
10 potential flow theory as illustrated in Fig. 1. It shows the vortex system with positive (downwards) flap deflection in spatial **(a)** and temporal **(b)** consideration.
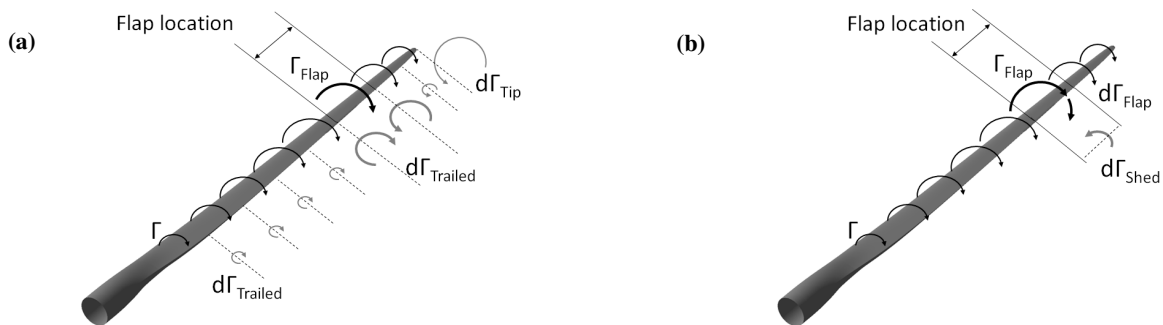
Figure 1. Sketch of the bound circulation along a wind turbine blade with trailing **(a)** and shed **(b)** vorticity

Due to the spatial gradient of bound circulation along the blade radius, a vortex sheet trails the rotor blade. In the flap section the bound circulation increases locally due to the change in camber. This leads to higher gradients at the flap edges and hence stronger trailing vortices at these locations. Outboard at the blade tip, the tip vortex is shown. Wake vorticity caused by radially
15 changing bound circulation is commonly referred to as trailed vorticity.

Generally the efficiency of the flap with regard to local lift increase or decrease is reduced by trailed vorticity in the 3D case. However, the blade parts next to the flap section produce a higher or lower lift for respectively positive or negative flap deflections. This is caused by the sign change of the induced velocities over the flap edge. With regard to integral loads such as power and thrust, this effect counters the negative impact of trailing vortices in the flap section.
20 The temporal consideration (Fig. 1b) displays an increase of bound circulation caused by an increase of the flap angle. This causes shed vorticity with opposed sense of rotation. Shed vortex structures re-induce velocities at the blade location and lead to a change in the effective angle of attack (AoA, α) which in turn influences in the blade loads. Wake vorticity linked to temporal changes in bound circulation is called shed vorticity.

Shed vorticity has been analyzed by Theodorsen and Garrick (1942) as well as by Leishman (1994) for the 2D case of an airfoil with flap. Theodorsen and Garrick derived an analytical solution for the unsteady lift response caused by sinusoidal flap actuation based on his theory from 1935 for thin airfoils (Theodorsen, 1935). This solution is dependent on the reduced frequency (Eq. (1)), one of the most important characteristic parameters when it comes to unsteady aerodynamics (Leishman, 2002). It is a measure of the unsteadiness of a problem as relation between frequency f and chord length c to the inflow velocity v_{inf}.

$$k = \frac{\pi \cdot f \cdot c}{v_{inf}} \qquad (1)$$

The derived function (Eq. (2)) consists of two terms: a first term which represents the circulatory forces connected to the bound circulation, and a second term which accounts for added mass effects. This second term is mostly referred to as non-circulatory part and depicts the influences of the inertia of the fluid. In this function β represents the instantaneous flap angle and its time derivatives. The coefficients F_1 to F_{11} are geometric terms solely dependent on the relative flap length to chord. For their definition it shall be referred to Leishman (1994). The function $C(k)$ is the complex Theodorsen function which accounts for the effects of the shed wake.

$$c_l(t) = \underbrace{2\pi C(k) \left(\frac{F_{10}\beta}{\pi} + \frac{F_{11}\dot{\beta}c}{4\pi v_{inf}} \right)}_{1} + \underbrace{\frac{c}{2v_{inf}^2} \left(-v_{inf}F_4\dot{\beta} - \frac{c}{2}F_1\ddot{\beta} \right)}_{2} \qquad (2)$$

The instantaneous lift coefficient $c_l(t)$ can be analyzed with regard to the amplitude Δc_l and phase shift ϕ of the lift response in relation to the input flap signal. Figure 2 shows the solution for a flap length of 10% chord as function of the reduced frequency k. In the diagram two curves are plotted: a solid curve which represents the solution of the complete function $c_l(t)$ and a dashed curve which shows the solution if only the circulatory components are regarded and apparent mass effects are neglected. No major difference between both curves is apparent in Δc_l. It is continuously decreasing with k in the displayed range which is applicable for this work as the investigated flap frequencies correspond to reduced frequencies of $k = 0.024 - 0.147$ at mid flap position. An increasing lag can be observed in phase shift, which is more pronounced if only circulatory components are included. While below a value of roughly 0.1 the differences between both curves are small, higher discrepancies are observed at larger k when apparent mass effects become increasingly dominant. In conclusion it is however found that the non-circulatory contribution is in the investigated range of reduced frequency of minor importance.

Theodorsen's derivations include the assumptions of thin airfoils and 2D flow. Both is not applicable for the aerodynamics of a modern wind turbine since current developments in blade design tend towards thicker airfoils for increased stiffness. But since the theory is well-known and commonly used to determine unsteady aerodynamic characteristics, it is compared to the obtained results.
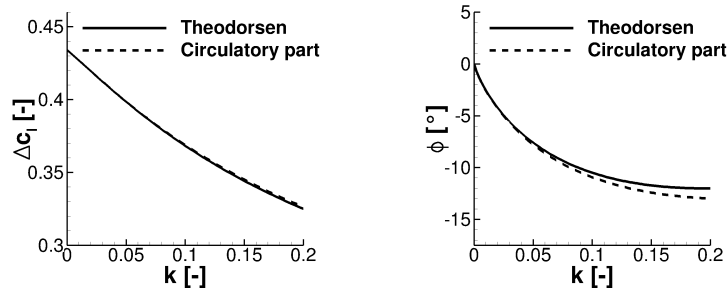
Figure 2. Lift amplitude and phase shift according to Theodorsen

3 Numerical approach

3.1 Simulation process chain

The process chain for the simulation of wind turbines, which was developed at the Institute of Aerodynamics and Gas Dynamics (IAG), University of Stuttgart (Schulz et al., 2016), is used in the present work. The main part constitutes the CFD code FLOWer

5 of the German Aerospace Center (DLR) (Kroll and Fassbender, 2002).

FLOWer is a compressible code that solves the 3D Reynolds-Averaged Navier-Stokes (RANS) equations in integral form. The finite-volume numerical scheme is formulated for block-structured grids. A second order central discretization with artificial damping is used to determine the convective fluxes, which is also called the Jameson-Schmidt-Turkel (JST) method. Transient simulations make use of the implicit Dual-Time-Stepping scheme. To close the RANS equation system, several state-

10 of-the-art turbulence models can be applied, as for example the SST model by Menter (1994) used in this study. FLOWer offers the use of the CHIMERA technique for overlapping meshes which is applied in the simulation of 3D wind turbines.

Grid generation is widely automated with scripts for 2D airfoils and 3D rotor blades. The generation of the blade grid for example is conducted with Automesh, a script developed at the IAG for the commercial grid generator Gridgen by Pointwise. The blade grids are of C-type with a tip block and coning towards the blade root in order to connect to the turbine spinner.

15 Spinner and nacelle are typically included in the simulations. In case of pure rotor simulations as performed in this study, the computational domain is modeled as a 120°-model with periodic boundary conditions on each side to reduce computing efforts. For the present study, this means that the flaps of all blades are deflected simultaneously.

On the post-processing side, again several scripts are available for the analysis of the simulations. Loads are calculated by the integration of pressure and friction distribution over the blade surface. Sectional distributions along the blade radius are

20 determined similarly by dividing the blade into different radial sections.

3.2 Trailing edge flap model

Trailing edge flaps are modeled based on grid deformation in FLOWer. Therefore, the deformation module (Schuff et al., 2014) was extended by a polynomial function ((Daynes and Weaver, 2012), (Madsen et al., 2010)) to describe the shape of the deflected flap.

$$
5 \quad w = \varphi(x) \cdot \beta \quad \varphi(x) = \begin{cases} 0 & 0 \le x < (c-b) \\ \frac{(c-x-b)^n}{b^{n-1}} & (c-b) \le x \le c \end{cases} \tag{3}
$$

In Eq. (3) c represents the chord length and b the flap length. The result w is the vertical change in y-direction, while the movement in x-direction is neglected for small deflection angles up to $10°$. Using this function requires the chord to be aligned with the x-axis. The polynomial order n is set to 2 for this investigation. In Fig. 3 the deformation methodology shown for a 2D airfoil section. The un-deformed and deformed airfoil surface are shown serving as input to the grid deformation algorithm,

10 which computes the new simulation grid at each time step.
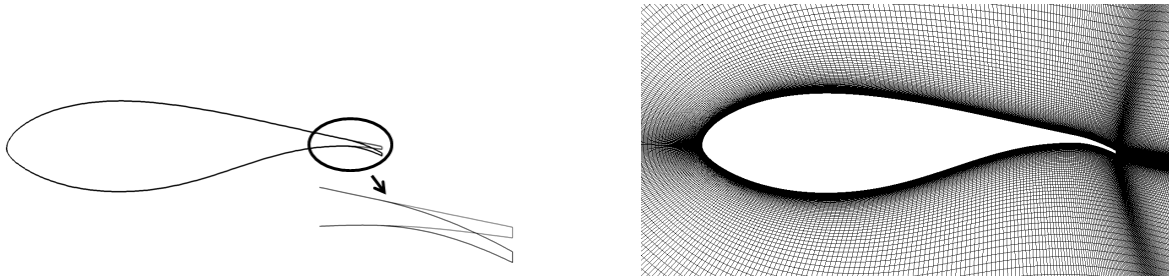
Figure 3. Methodology for 2D deflection (Jost et al., 2016)

The approach for the blade mesh is displayed in Fig. 4. There is no separate grid for the flap part. It is integrated into the blade grid. The connection between the moving flap part and the remaining rigid blade surface is computed by the deformation algorithm which generates a smooth transition. At the location of these transitions the blade grid is radially refined to capture gradients in the flow field which are expected to occur.

15 ## 3.3 Code-to-code validation of the simulations

A baseline simulation setup for the DTU 10 MW turbine without flap has been examined and validated by code-to-code comparison within the European FP7 project AVATAR. For this purpose a simulation of the power curve on the basis of the stiff straight blade without precone was conducted in steady mode. The comparisons between the different codes of the project partners is presented in (Sørensen et al., 2015). The FLOWer results showed a good accordance with results obtained

20 with EllipSys3D by DTU and MapFLow by NTUA. A detailed analysis of the FLOWer results with a special focus on the
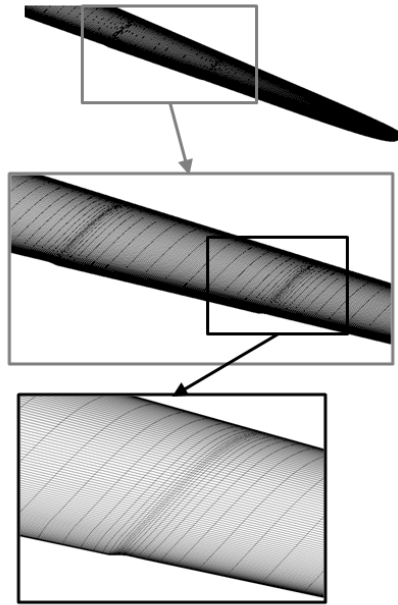
Figure 4. Methodology for 3D deflection

comparison of steady and unsteady simulations is performed in (Jost et al., 2015b). A comparison of the simulations with flaps
to the AVATAR project partners can be found in (Ferreira et al., 2015) and (Aparicio et al., 2016).

3.4 Grid generation

For the 2D airfoil simulations, the 75% blade cut of the DTU 10 MW turbine (FFA-w3-241 airfoil), which is the mid flap

5 position in the chosen trailing edge flap configuration, was extracted from the geometry. The airfoil grid was generated using a
script for the commercial grid generator Pointwise. Approximately 180,000 grid cells have been used with 417 surface nodes
and 205 nodes in wall-normal direction. Boundary layer resolution was chosen for $y^+ < 1$ and the farfield boundary is located
at 150 chords distance.

For the rotor simulations the setup used in the code-to-code validation was modified in order to simulate the rotor with

10 trailing edge flap. Flap edge refinements were included into the blade grid and a higher resolved background grid was chosen
to accurately capture wake effects. A separate grid convergence study of the blade grid was performed with a steady flap
deflection +/- 10° and the results are presented in (Jost et al., 2015a). The final setup used in the present study amounts
approximately 21.65 million cells. The distribution between the different grids is shown in Table 1.

Table 1. Grid cells in the 120°-model

Blade	Spinner	Nacelle	Background	Total
8.16e6	1.39e6	1.45e6	10.65e6	21.65e6

3.5 Temporal discretization of the simulation setup with flaps

Another critical issue with regard to the unsteady simulations is the temporal resolution meaning the choice of time step. Unsteady simulations in FLOWer make use of the Dual-Time-Stepping method as implicit scheme. In this approach a pseudo-time is introduced into the equation system at each time step for which a steady solution is obtained. The method allows the
5 choice of significantly larger time steps than those dictated by the CFL condition in explicit schemes. However, the actual eligible size is problem dependent. In most cases the time step is a trade-off between simulation accuracy and computational time and it is necessary to determine the largest possible time step that can still resolve the unsteady flow effects sufficiently. To analyze the influence of the temporal discretization within this study, a sensitivity study has been performed based on 2D and 3D simulations

10 At first the 2D airfoil case (FFA-w3-241) is presented. The simulations have been performed at realistic inflow conditions extracted from the 3D rotor case to connect 2D and 3D results. The Reynolds number was determined to 15.4 millions, Mach number to 0.2 and the AoA to 6.5°. For the determination of the time step influence the high flap frequency corresponding to the sixth of the rotational velocity at rated operational point (6p) was chosen, which corresponds to a reduced frequency of 0.147. Results for the lift coefficient c_l and drag coefficient c_d are shown in Fig. 5. Four different time steps have been selected
15 for the study and 100 inner iterations are performed in the Dual-Time-Stepping scheme for all investigated time steps except the small step of 0.028° for which 30 inner iterations are regarded sufficient. As the results are transferred to the 3D case later on, the different time steps are designated by the corresponding azimuth step in a rotor simulation at rated rotational speed. A time step of 0.028° is for example equivalent to 4.8e-4 s. This very small step correlates to 100 steps per convective time unit, which is in this case the chord length. With regard to the computational effort this time step is not realizable for the 3D case,
20 but serves as reference in this 2D study. All other discretizations are applicable for pure rotor simulations. In both aerodynamic coefficients the influence of the time step size is apparent, but the effect on drag is more distinct. While lift agrees well for all resolutions except for 1°, drag shows noticeable differences at 0.5° and minor differences at 0.25°.

Another parameter of influence is the amount of inner iterations in the Dual-Time-Stepping scheme which is analyzed for the time step of 0.5° with three different amounts of inner iterations, 50, 100 and 200. The results are displayed in Fig. 6. Again
25 the results for the small time step of 0.028° is shown as reference.

Generally, it is observed that the temporal accuracy is more dependent on the total amount of iterations per convective unit, than the choice of time step or inner iterations. By comparing the plots in Fig. 5 and Fig. 6, it can be seen that for example the hysteresis for 1° and 100 inner iterations is very similar to the curve with 0.5° and 50 inner iterations. This conclusion can however not be transferred to separated flows, for which a small time step is needed to resolve effects correctly.
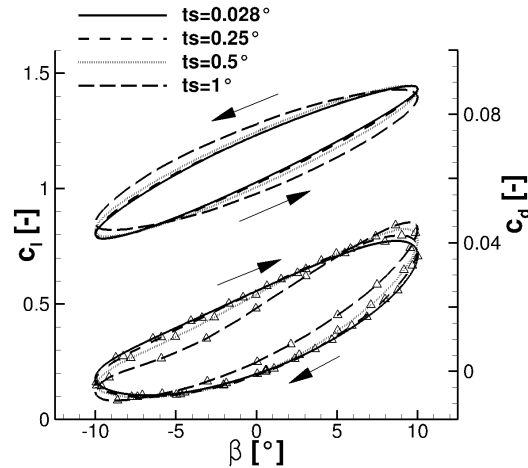
Figure 5. 2D Influence of time step, lift (no symbol) and drag (symbol △)
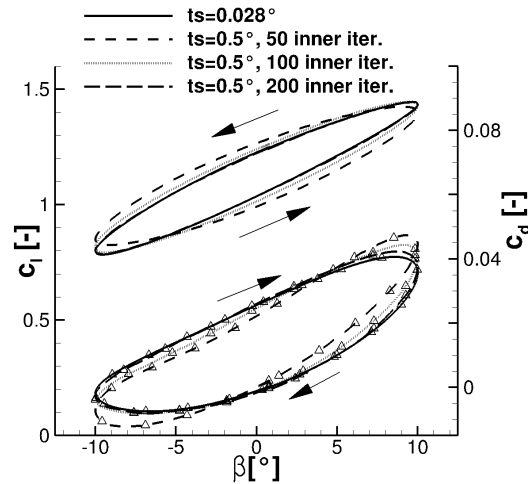
Figure 6. 2D Influence of inner iterations, lift (no symbol) and drag (symbol △)

Based on these outcomes, simulations of the rotor model have been conducted in order to get an impression of the 3D case. The flap is again oscillating with 6p frequency at rated operational condition. Similar time step sizes as in the 2D case have been chosen replacing 0.028° with 0.125° as further halving. 100 inner iterations are used. Figure 7 shows the resulting driving force and thrust variations at mid flap position.

5   The forces are normalized with the total mean value to allow an easier assessment of the differences. While thrust shows a good agreement for all time step sizes, higher deviations are observed in the driving component in which the drag differences have a stronger impact. However a convergence of the curve progressions with decreasing time step size can be observed leading to small differences between 0.125° and 0.25°.
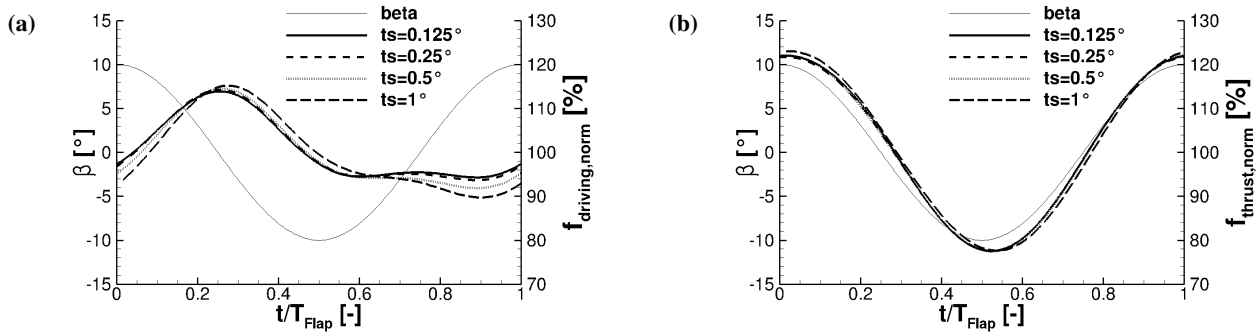
Figure 7. 3D influence of time step, 6p, 75% blade cut, normalized driving force **(a)** and thrust **(b)**

To conclude the temporal discretization study, a time step size of 0.25° with 100 inner iterations for a flap frequency 6p shows sufficient accuracy in 3D simulations as trade off to computational time. This corresponds to 240 steps per flap oscillation. In 2D simulations smaller time steps correlated to the convective unit are feasible and consequently used.

4   Results

5 ### 4.1   3D rotor simulations with oscillating flap

At first, results of the different flap frequencies are compared for the 3D rotor simulations. All simulations have been conducted at rated conditions with 11.4 m/s wind speed and 9.6 rpm. The blade pitch angle is set to 0°. As ambient conditions an air density of 1.225 kg/m³ and a temperature of 288.15 K are used. The simulations were started as steady state computation on two multi grid levels with 8000 iterations respectively and a flap angle of 0°. This steady solution is then restarted in unsteady mode and 10 simulated for the amount of revolutions required for converged loads. With regard to the Menter SST turbulence model it has to be mentioned that the required wall distances of each cell were computed only once at the simulation start and not updated every time step. This was done since only minor influence was found in 2D airfoil simulations and to save computation time as in 3D the wall distance calculation is very time consuming. Please note that while in the previous time step study a cosine function is used as deflection signal, now a sinus function is applied (Eq. (4)).

15 $$\beta(t) = 10° \cdot sin\left(2\pi t \frac{N}{T_{Rotor}}\right) \qquad\qquad N = [1, 2, 3, 6], \ T_{Rotor} = 6.25s \qquad\qquad (4)$$

The flap frequencies correspond to reduced of frequencies of $k = 0.024(1p) - 0.147(6p)$ at mid flap position. Figure 8 shows the results of integral power and thrust plotted over one rotor revolution. The effect of the flap can be seen clearly in both diagrams. Power and thrust are oscillating with the respective frequency. A higher frequent fluctuation is also apparent in the graphs, which results from unsteady flow separation at the cylindrical blade root. As illustrated in the streamlines plot on 20 the blade surface shown in Fig. 9, flow separation is dominant there.
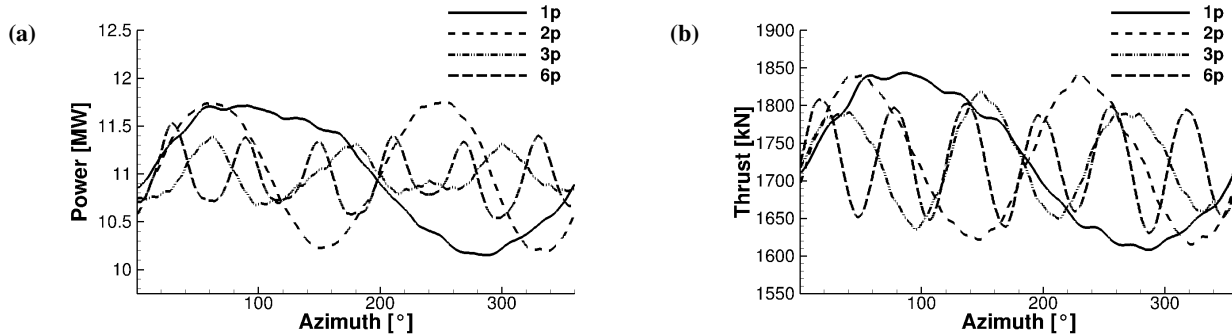
Figure 8. Integral rotor power **(a)** and thrust **(b)**

Figure 9. Blade root flow separation - pressure side

Due to this superposition of effects in the integral forces, it is necessary to regard sectional forces at a blade cut belonging to the flap part in order to investigate the flap effects. In the following like in the time step study the 75% cut as mid flap position was extracted from the simulations. Figure 10 shows the results of the local driving force and thrust at this location. While thrust shows the expected amplitude decrease and higher phase shifts with increasing frequency, larger differences are observed in the driving component. For the 3p and 6p case a second superimposed oscillation is visible from $t/T_{Flap} \approx 0.8 - 1.2$ (respectively 0.2 in Fig. 10a). This results from the high impact of drag at rated condition. As seen above (Fig. 5), drag shows a significant amplitude increase at higher frequencies and additionally c_l and c_d experience a different phase shift. The superposition of the in-plane force components leads to this phenomenon.

In Fig. 11 and Fig. 12 sectional distributions of driving force and thrust are shown for 1p and 6p case respectively. Four instantaneous solutions are plotted for maximum, minimum and 0° flap deflection over the blade radius. Once more the strong influence of drag on the driving component can be seen. For maximum positive deflection ($t/T_{Flap} = 0.25$) the related drag increase causes a driving force reduction in the flap section. The change of sign in induced velocity caused by the flap edge vortices is also apparent in the driving force as significant steps appear at the transition between flap and rigid rotor part. In both force components the positive effect of the flap deflection on neighboring blade sections can be seen as it is described in
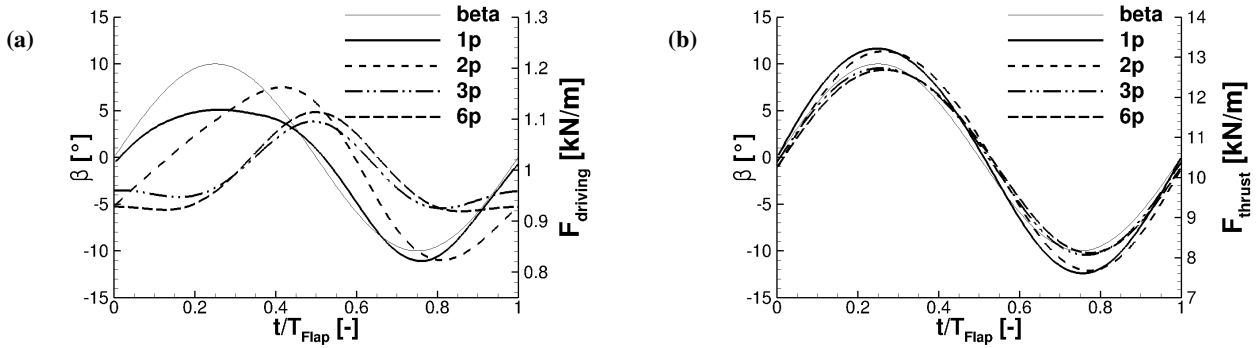
Figure 10. Variation of flap frequency, 75 % blade cut, driving force **(a)** and thrust **(b)**

Sect. 2. While trailing vorticity reduces the effect of the flap in the flap section compared to 2D, the sections next to the flap part produce higher/lower lift due to the induced upwind/downwind for respectively positive/negative flap angles.
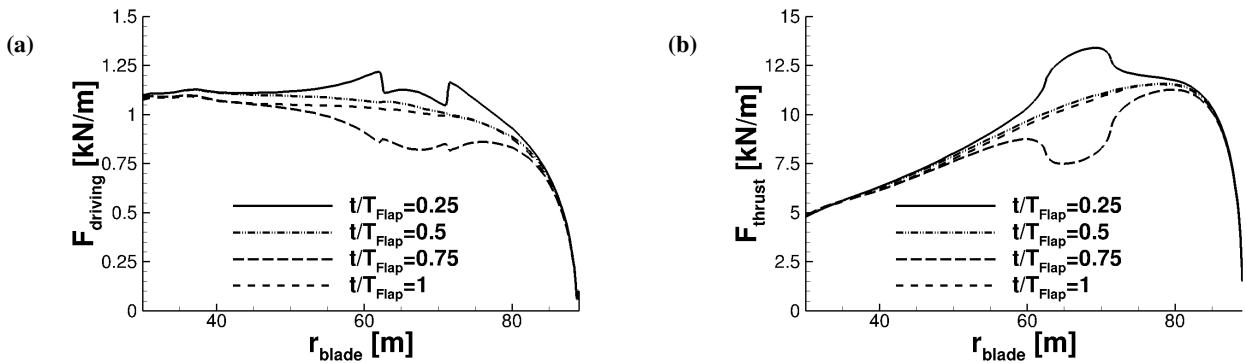
Figure 11. 1p sectional forces (driving force **(a)** and thrust **(b)**)
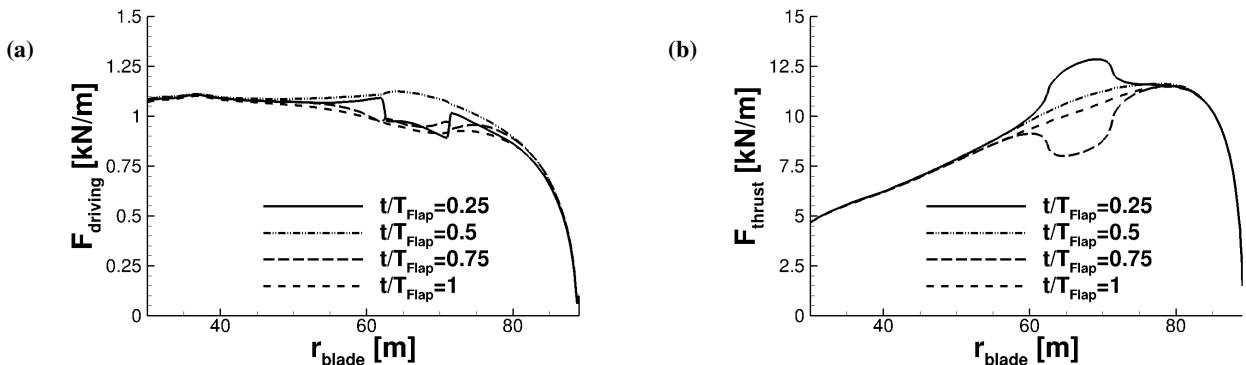
Figure 12. 6p sectional forces (driving force **(a)** and thrust **(b)**)

The differences caused by unsteady effects can also be observed in the plots. Larger variations of the forces are seen in the 1p case compared to the 6p case over the whole blade part influenced by the flap. The hysteresis can especially be noticed at the time instance when the flap is positioned at $0°$ deflection. While in the 1p case the sectional loads at increasing or decreasing flap angle are closely together, in the 6p case larger differences are seen. For the decreasing flap angle at $t/T_{Flap} = 0.5$ the loads are higher than for the increasing flap angle at $t/T_{Flap} = 1$.

4.2 Comparison to steady flap deflections

In a first step to analyze the influence of unsteady effects in 3D, the results are compared to the simulations of steady flap deflection for +/-10°. Table 2 presents the resulting integral loads. Like for the oscillating flap cases the simulations were initiated in steady state and then restarted in unsteady mode for three turbine revolutions. The table shows mean values of the third revolution.

Table 2. Integral for steady/no flap deflection

	$\beta = 10°$	$\beta = 0°$	$\beta = -10°$
Power [MW]	10.75	11.13	10.94
Thrust [kN]	1793	1738	1654

By comparing to the results of the oscillating flap (Fig. 8), it can be noticed that in the oscillating cases an increase of power is possible, while for steady deflections this is not the case. A negative flap angle even leads to a higher power output than a positive deflection. This phenomenon is caused by the differences in axial induction. For positive deflections c_l increases, more energy is extracted from the wind and consequently the axial inductions also rises. This leads to a lower angle of attack at the rotor blades, which reverses the effect of the flap with regard to power. The opposite is observed in case of negative flap angles. But since less energy is extracted from the wind, still a lower power output compared to the neutral flap case is observed. In this background thrust also shows reasonable values. The magnitudes in the steady cases are lower compared to the 1p oscillating case, for which the axial induction is not able to fully adjust to the changed load situation and consequently higher oscillations are possible.

To verify this hypothesis an extraction of the local AoA along the blade radius has been performed according the reduced axial velocity method (Johansen and Sørensen, 2004). This method has proven to show reasonable results (Jost et al., 2016), but is only applicable for steady inflow conditions. But since in the 1p case the reduced frequency is still very low with a value of 0.024 at mid flap position, a quasi-steady approach is appropriate. The method requires annular elements at different radii in front and behind the rotor plane as input. These elements are placed at an axial distance of one local chord to the rotor blade for the present evaluation. The choice of this axial distance has however shown to have an influence on the results with maximum discrepancies of about $0.16°$ when the axial distance is reduced for example to 0.2 local chords. Nevertheless, the results of the different cases can be compared to each other and give a qualitative and within this tolerance quantitative analysis.

The plot displayed in Fig. 13 highlights the differences for steady and oscillating flap deflections and underlines that in unsteady cases the axial induction is only slowly adjusting. Consequently dynamic inflow effects play an important role on trailing edge flaps, especially at lower flap frequencies.
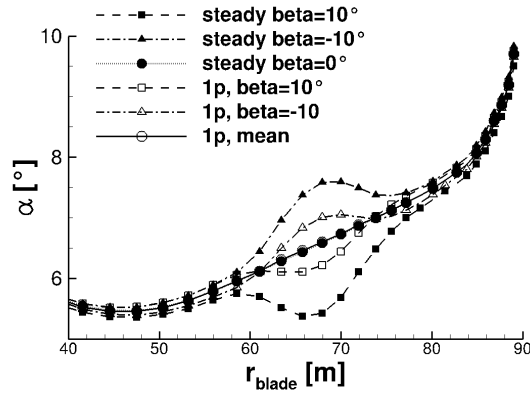
Figure 13. Extracted AoA according to Johansen and Sørensen (2004)

Figure 14 and Fig. 15 show extracts from the flow field at an axial distance of one local chord in front and behind the rotor
5 blade for respectively maximum positive and flap negative angle.
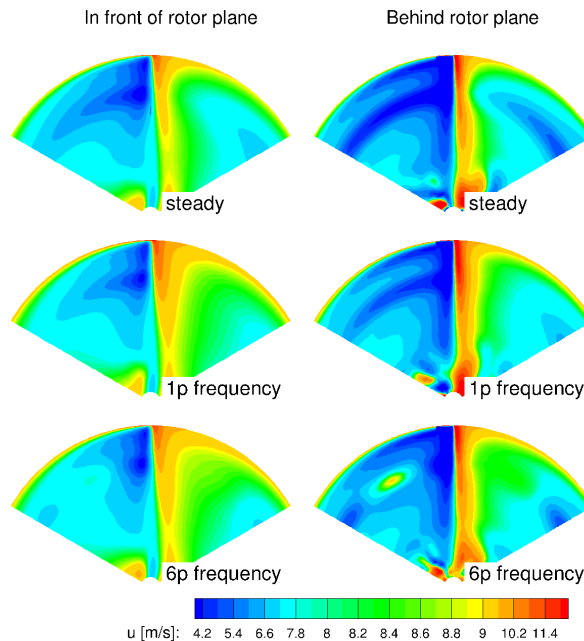
Figure 14. Flow field extracted at one local chord distance in front and behind the rotor blade for $\beta = 10°$
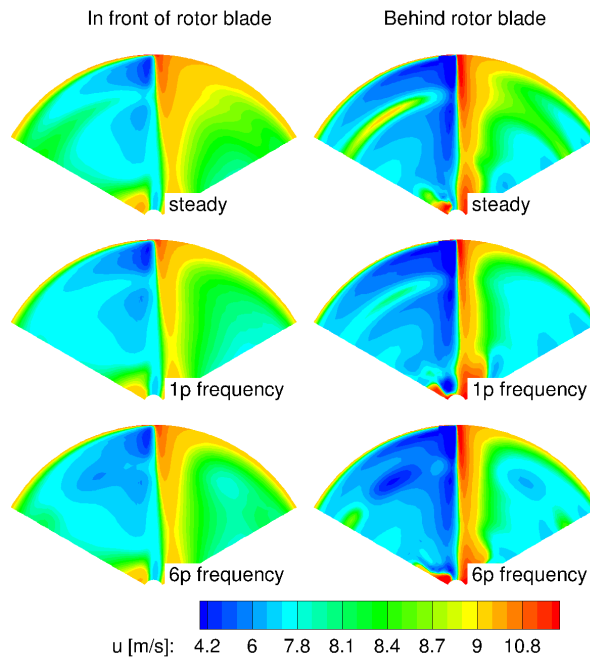
Figure 15. Flow field extracted at one local chord distance in front and behind the rotor blade for $\beta = -10°$

The contour of the axial velocity u is displayed from a front view to the turbine which means that the rotational direction is clockwise. The rotor blade is positioned upright. In each figure three cases are shown, steady flap deflection, 1p oscillation and 6p oscillation. Clearly the flow acceleration towards the blade and the reduction of the wind speed in the blade wake can be seen in all cases. In the flap section the opposing deflection can mainly be identified in the blade wake, where less reduction is observed for a negative angle and a higher reduction for a positive angle. By comparing steady deflections to the 1p frequency the different axial induction can be seen. When comparing the 1p and 6p frequency, the different flap frequencies can also be noticed in the blade wake. In the 6p case at for example $\beta = 10°$ an area with increased velocity is apparent.

4.3 Influence of varying angle of attack in 3D

To analyze the influence of the varying AoA for the oscillating flap cases, again the 1p is regarded in the following for which it is most pronounced. For this purpose the results of the AoA extraction with the reduced axial velocity method are regarded at mid flap position over on flap period. The variation of the local inflow velocity and the AoA is shown in Fig. 16. While the inflow velocity shows no major variations, the AoA oscillates with an amplitude of 0.6°.

Figure 17 presents the resulting c_l and c_d variations in addition to the resulting variations for an averaged angle of attack of 6.5° and inflow velocity of 68 m/s ($c_{l,mean}$, $c_{d,mean}$). It can be seen that the AoA oscillations have only a minor influence on the value of c_l but strongly on c_d. This is reasonable as for the determination of c_l and c_d in the 3D case, the forces are integrated from the surface solution as driving force and thrust component at first and then transferred to the local inflow or
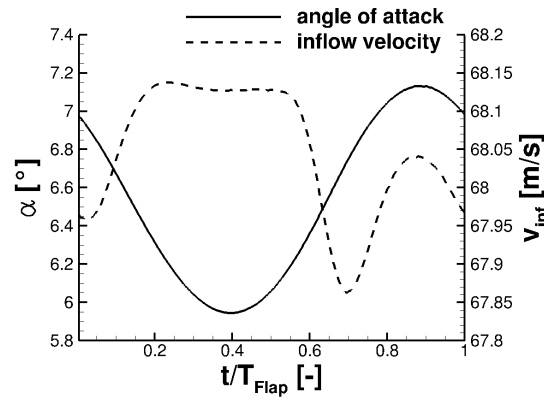
Figure 16. 1p Instantaneous inflow conditions 3D, 75 % radius.

also called aerodynamic coordinate system. The procedure is shown in Fig. 18 for both components. To determine total lift and drag forces both shares by driving force and thrust are summed up.
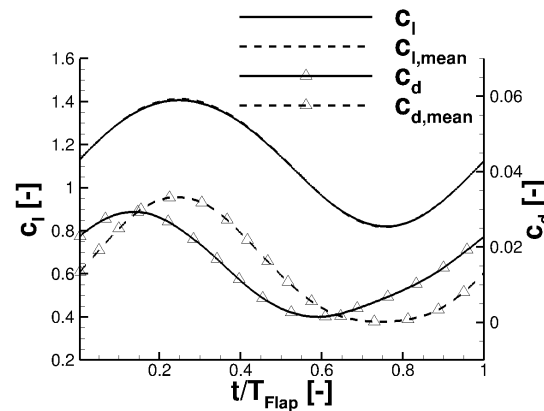
Figure 17. 1p Comparison of lift and drag, 3D instantaneous/ 3D mean, 75 % radius.

As the value of c_l is roughly 100 times larger compared to c_d, a projection difference of 0.6° as observed in the 1p case has only a negligible impact on c_l. Consequently the results for c_l and $c_{l,mean}$ are very similar. c_d is however strongly differing and therefore it is not possible to draw any conclusions on c_d without knowing the precise transient AoA in the 3D case. An accurate AoA determination, especially in unsteady simulations, is however very delicate as trailed and shed vorticity needs to be accurately considered. Further research is needed in this field to be able to conduct such analyses. With regard to c_l the differences are however small and also the average approach is considered appropriate within certain limitations. This allows the analysis of the higher flap frequencies for which the reduced axial velocity method is not applicable.
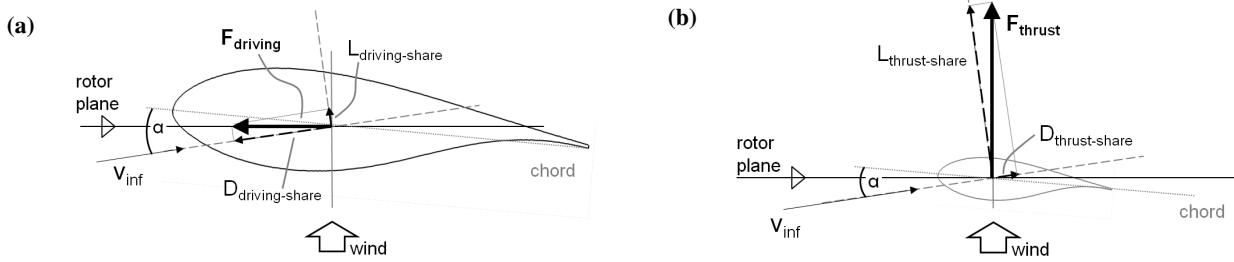
Figure 18. Transformation of driving force and thrust to local aerodynamic coordinate system (driving force **(a)** and thrust **(b)**)

In order to quantify the limitations of the average approach a FFT analysis of the results has been performed for the 1p frequency and the main peak in frequency is analyzed. The averaged and instantaneous solution differ by only 1% in lift amplitude and 0.26° in phase shift, which is below the time step resolution of 1.5°. In the following comparison to 2D simulations the main focus point is hence to assess the change of lift amplitude. Due to the limitations caused by the time step hysteresis
5   effects are only qualitatively judged by comparing the curves.

4.4   Comparison to 2D simulations

To study the unsteady phenomena in more detail and to analyze the main effects in the 3D case, the instantaneous $c_{l,mean}$ results of the 3D extraction are compared to 2D airfoil simulations of the mid flap position at mean inflow conditions. The mean inflow conditions used as input for all flap frequencies in 2D are again: $AoA = 6.5°$ and $v_{inf} = 68m/s$. This leads to a
10   Mach number of 0.2 and a Reynolds number of 15.4 million.

Results of the comparison between 2D static deflection, 2D sinusoidal deflection and 3D sinusoidal deflection are shown in Fig. 19. In order to get an impression of the influence of AoA oscillation in the 1p case, additionally an AoA corrected version of the 2D sinusoidal oscillation case is plotted which is computed by Eq. (5).

$$c_{l,2Dsinus,AoAcorr}(t) = c_{l,2Dsinus}(t) + 2\pi\left(\alpha_{3Dsinus}(t) - \alpha_{mean}\right) \tag{5}$$

15   As for the higher frequencies the reduced axial velocity method is not applicable but also as the AoA variations are smaller compared to the 1p case, no AoA corrected curve is plotted. For these cases the results obtained with the 2D theory of Theodorsen have been added. The plots show the expected decrease of lift amplitude from 2D static over 2D sinusoidal to 3D sinusoidal. For the 1p oscillation the comparison of 2D static and 2D sinusoidal results shows the minor influence of unsteady effects. Even though a beginning hysteresis is seen in the 2D sinusoidal results, c_l amplitude reduction is still small.
20   This result corresponds well to the low reduced frequency in this case of 0.024. Larger differences are seen by comparing 2D and 3D results which show the decrease of amplitude caused by trailing and shed vorticity. The reduced amplitude leads to less shed vorticity and thus less hysteresis is apparent compared to the 2D solution.
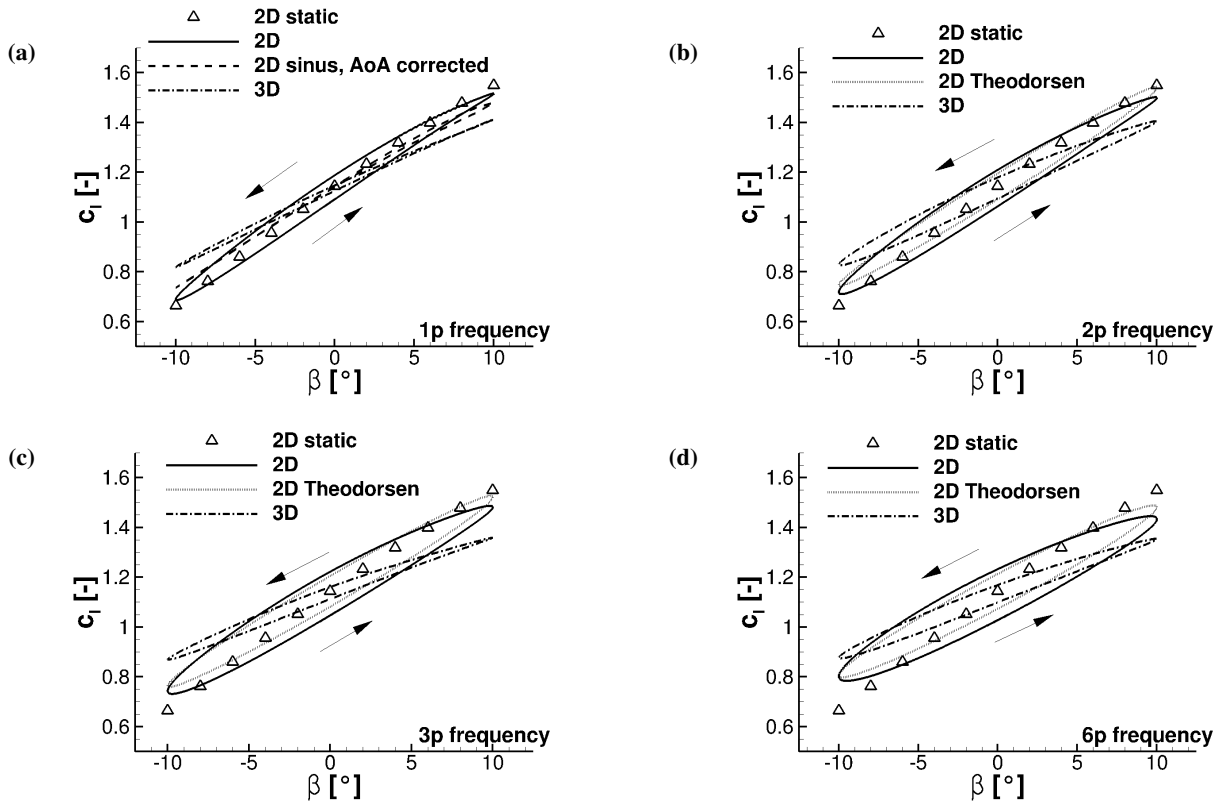
Figure 19. Comparison of 2D/3D lift for different flap frequencies: 1p **(a)**, 2p **(b)**, 3p **(c)** and 6p **(d)**

The AoA corrected 2D curve shows the approximate result for a 2D simulation including an AoA variation in the inflow. The curve demonstrates less hysteresis and a smaller amplitude compared to the baseline progression, which is reasonable since the AoA progression is a feedback of the aerodynamic forcing in the 3D case. Like it was noticed in Sect. 4.2, for low flap frequencies the axial induction is able to react to the instantaneous load and mimics the effects. The smaller slope which is seen in the 3D curve can be explained by the decrease of the gradient $dc_l/d\beta$ caused by trailing vortices in 3D.

In 2D unsteady effects constantly increase with the flap frequency for the regarded cases what corresponds well to the results with Theodorsen's 2D theory. The amplitude of lift oscillation is continuously reducing and more pronounced hysteresis are seen. The results obtained with the Theodorsen theory are in fair agreement to the CFD results. A more symmetrical hysteresis is apparent compared to the slightly bent CFD curves. Generally the hysteresis direction is in agreement to the observations made by Troldborg (2005). In 3D the amplitude is also continuously decreasing but hysteresis effects show no clear trend. A slightly bigger hysteresis is seen for the 2p frequency than for the 3p frequency. A reason for this phenomena could be a different phase lag in the angle of attack oscillation resulting from the flap deflection. For clarification an AoA extraction for unsteady cases would be required.

Table 3 lists amplitudes and Table 4 phase lags of the lift coefficient for the different cases in order to quantify the effects. The values were again obtained by applying a Fast-Fourier transformation on the unsteady lift progression and analyzing the main peak in the results. Additionally results of the 2D theory by Theodorsen described in Sect. 2 are shown in the table. The results of this simplified theory are in a very good agreement to the results of 2D simulations with regard to the c_l amplitude.

5 Only at 6p a slight difference is noticeable. Larger differences are observed in the phase shift, for which higher values are determined in the 2D CFD simulation. These differences can be caused by the assumption of thin airfoils in Theodorsen's theory as similar observations were found by Motta et al. (2015) for pitching airfoils.

Table 3. c_l amplitude, 75% blade cut, 2D and 3D results

	1p	2p	3p	6p
2D	0.42	0.40	0.38	0.33
3D	0.30	0.29	0.25	0.24
$\Delta c_{l,3D}/\Delta c_{l,2D}$	71%	70%	66%	73%
2D, Theodorsen	0.42	0.40	0.38	0.35

Table 4. c_l phase shift, 75% blade cut, 2D results

	1p	2p	3p	6p
2D	-6.3	-10.2	-12.9	-17.7
2D, Theodorsen	-4.9	-7.5	-9.2	-11.7

The comparison of 2D and 3D results with regard the lift amplitude shows the expected decrease due to the influence of trailing vortices. The amplitude reduces to 66% to 73% of the result of 2D simulations at the same frequency. This percentual

10 reduction is relatively constant throughout all frequencies and is also found very similar for steady deflections (Jost et al., 2016). This leads to the conclusion that as first estimation the impact of trailing vortices for a certain flap configuration can be investigated in steady mode. Unsteady effects can be investigated separately in 2D and can then be superimposed with the 3D result.

5 Conclusions

15 In the present work the influence of unsteady 3D effects on trailing edge flaps has been investigated for the case of harmonic oscillations of the flap angle. For this purpose four different flap frequencies ranging from 1p to 6p of the rotational frequency were simulated on a 2D airfoil and 3D rotor. The simulations of the 3D rotor showed a significant influence of trailing and shed vorticity. This leads to a reduction of the amplitude and a phase lag in the load response to the flap signal with increasing flap

frequency. This behavior was observed in both, integral and sectionally distributed forces along the blade radius. The negative influence of trailing vortices in the flap section is however partly compensated by an increased efficiency of neighboring sections due to the induced up- or downwind. A high impact of dynamic inflow effects is observed in the comparison to steady flap deflection. Unlike in the oscillating cases the axial induction of the turbine is able to fully adjust to the changed load

5   situation for steady flap deflections which results in the rotor loads.

A detailed investigation of the 75% blade cut representing the mid flap position was performed in order to compare 2D airfoil to 3D rotor results and thereby quantify unsteady 2D and 3D effects. The 2D CFD simulation were additionally compared to the simplified model by Theodorsen, a widespread analytical approach for this matters. A good agreement between 2D CFD and the Theodorsen model were observed with regard to the amplitude of the lift oscillations. Higher discrepancies could be

10   noticed in the phase shift which could be assigned to Theodorsens assumption of thin airfoils. The comparison of the 2D and 3D CFD simulations revealed the significantly higher reduction of the lift amplitude in the 3D rotor case due to trailing vorticity. Only about 70% of the 2D value for the respective flap frequency is achieved. Additionally less hysteresis is seen at the rotor blade which is connected to the decrease of lift amplitude.

Acknowledgements. The authors acknowledge European FP7 project Innwind.EU for funding (Grant agreement No. 308974). This work

15   was partly performed on the Supermuc Cluster (LRZ Munich), the HazelHen and NEC Cluster (HLRS Stuttgart) and the bwUniCluster (framework bwHPC, funding: Ministry of Science, Research and Arts and the Universities of the state Baden-Württemberg).

References

Aparicio, M., Martín, R., Muñoz, A., and González, A.: AVATAR D3.3 - Results of a parametric study of flow devices, guidelines for design, Tech. rep., AVATAR project, 2016.

Bak, C., Zahle, F., Bitsche, R., Kim, T., Yde, A., Henriksen, L., Andersen, P., Natarajan, A., and Hansen, M.: Design and performance of a 10 MW turbine, Tech. rep., DTU, dtu-10mw-rwt.vindenergi.dtu.dk, 2013.

Barlas, T., van der Veen, G., and van Kuik, G.: Model predictive control for wind turbines with distributed active flaps: incorporating inflow signal and actuator constraints, Wind Energy, 15, 757–771, doi:10.1002/we.503, 2012.

Castaignet, D., Barlas, T., Buhl, T., Poulsen, N., Wedel-Heinen, J., Olsen, N., Bak, C., and Kim, T.: Full-scale test of trailing edge flaps on a Vestas V27 wind turbine: active load reduction and system indentification, Wind Energy, 17, 549–564, doi:10.1002/we.1589, 2014.

Daynes, S. and Weaver, P.: A morphing trailing edge device for a wind turbine, Journal of Intelligent Material Systems and Structures, 23, 691–701, doi:10.1177/1045389X12438622, 2012.

Ferreira, C., Gonzalez, A., Baldacchino, D., and Aparicio, M.: AVATAR D3.2 - Development of aerodynamic codes for modelling of flow devices on aerofoils and rotors, Tech. rep., AVATAR project, 2015.

Johansen, J. and Sørensen, N.: Aerofoil characteristics from 3D rotor CFD simulations, Wind Energy, 7, 283–294, doi:10.1002/we.127, 2004.

Jost, E., Barlas, T., Riziotis, V., and Navalkar, S.: Innwind D2.3.2 - Validation of New Control Concepts by Advanced Fluid-Structure Interaction Tools, Tech. rep., Innwind.EU project, 2015a.

Jost, E., Lutz, T., and Krämer, E.: Steady and unsteady CFD power curve simulations of generic 10 MW turbines, in: Proceedings of the 11th PhD Seminar on Wind Energy in Europe, 2015b.

Jost, E., Lutz, T., and Krämer, E.: A parametric CFD study of morphing trailing edge flaps applied on a 10 MW offshore wind turbine, Energy Procedia, 94, 53–60, doi:10.1016/j.egypro.2016.09.192, 2016.

Kroll, N. and Fassbender, J.: MEGAFLOW – Numerical Flow Simulation for Aircraft Design, Springer, 2002.

Leishman, J. G.: Unsteady Lift of a Flapped Airfoil by Indicial Concepts, Journal of Aircraft, 31, 288, doi:10.2514/3.46486, 1994.

Leishman, J. G.: Challenges in Modelling the Unsteady Aerodynamics of Wind Turbines, Wind Energy, 5, 85–132, doi:10.1002/we.62, 2002.

Madsen, H., Andersen, P., Andersen, T., Bak, C., and Buhl, T.: The potentials of the controllable rubber trailing edge flap (CRTEF), in: Proceedings of the EWEC, 2010.

Menter, F. R.: Two-Equation Eddy-Viscosity Turbulence Models for Engineering Applications, AIAA Journal, 32, 1598–1605, 1994.

Motta, V., Guardone, A., and Quaranta, G.: Influence of airfoil thickness on unsteady aerodynamic loads on pitching airfoils, J. Fluid Mech., 774, 460–487, 2015.

Schuff, M., Kranzinger, P., Keßler, M., and Krämer, E.: Advanced CFD-CSD coupling: Generalized, high performant, radial basis function based volume mesh deformation algorithm for structured, unstructured and overlapping meshes, in: 40th European Rotorcraft Forum, Southhampton, 2014.

Schulz, C., Letzgus, P., Lutz, T., and Krämer, E.: CFD study of yawed inflow on loads, power and near wake of a generic wind turbine, Wind Energy, doi:10.1002/we.2004, 2016.

Sørensen, N., Hansen, N., Garcia, N., Florentie, L., Boorsma, K., Gomez-Iradi, S., Prospathopoulus, J., Barakos, G., Wang, Y., Jost, E., and Lutz, T.: AVATAR D2.3 - Power curve predictions, Tech. rep., AVATAR project, 2015.

Theodorsen, T.: General Theory of Aerodynamic Instability and the Mechanism of Flutter, Tech. Rep. 496, NACA, 1935.

Theodorsen, T. and Garrick, I. E.: Nonstationary flow about a wing-aileron-tap combination including aerodynamic balance, Tech. rep., NACA, 1942.

Troldborg, N.: Computational study of the Risø-B1-18 airfoil with a hinged flap providing variable trailing edge geometry, Wind Engineering, 2, 89–113, 2005.